Ice shelf basal melt rates in the Amundsen Sea at the end of the 21st century

Nicolas C Jourdain[1,1], Pierre Mathiot[2,2], Clara Burgard[2,2], Justine Caillet[2,3], and Christoph Kittel[2,2]

[1]French National Centre for Scientific Research (CNRS)
[2]Univ. Grenoble Alpes/CNRS/IRD/G-INP
[3]Université Grenoble Alpes/CNRS/IRD/G-INP, IGE, Grenoble, France

November 30, 2022

Abstract

Antarctic Ice Sheet projections show the highest sensitivity to increased basal melting in the Amundsen Sea sector. However, little is known about the processes controlling future increase in melt rates. We build an ensemble of three ocean–sea-ice–ice-shelf simulations for both the recent decades and the late 21st century, constrained by regional atmosphere simulations and the multi-model mean climate change of the 5th Climate Model Intercomparison Project under the RCP8.5 scenario. The ice shelf melt rates are typically multiplied by 1.4 to 2.2 from present day to future, for a total basal mass loss increased by 347Gt/yr. This is approximately equally explained by advection of warmer water from remote locations and by regional changes in Ekman downwelling and in the ice-shelf melt-induced circulation, while increased iceberg melt plays no significant role. Our simulations suggest that high-end melt projections previously used to constrain recent sea level projections may have been significantly overestimated.

Ice shelf basal melt rates in the Amundsen Sea at the end of the 21$^{\mathrm{st}}$ century

Nicolas C. Jourdain[1], Pierre Mathiot[1], Clara Burgard [1], Justine Caillet[1], Christoph Kittel[1]

[1]Univ. Grenoble Alpes/CNRS/IRD/G-INP, Institut des Géosciences et de l'Environnement, Grenoble, France

Key Points:

- We present 1/12° ocean–sea-ice–ice-shelf projections at the end of the 21$^{\mathrm{st}}$ century under the RCP8.5 scenario.
- Ice shelf melt rates in the Amundsen Sea are typically multiplied by 1.4 to 2.2 from 1989–2009 to 2080–2100.
- Advection of warmer water from remote locations and reduced Ekman downwelling are the main drivers of changes in ice shelf melt rates.

Corresponding author: Nicolas C. Jourdain, `nicolas.jourdain@univ-grenoble-alpes.fr`

Abstract

Antarctic Ice Sheet projections show the highest sensitivity to increased basal melting in the Amundsen Sea sector. However, little is known about the processes that control future increase in melt rates there. We build an ensemble of three ocean–sea-ice–ice-shelf simulations for both the recent decades and the late 21st century, constrained by regional atmosphere simulations and the multi-model mean climate change of the 5th Climate Model Intercomparison Project under the RCP8.5 scenario. The ice shelf melt rates are typically multiplied by 1.4 to 2.2 from present day to future, for a total basal mass loss increased by 347 $\mathrm{Gt\,yr^{-1}}$. This is approximately equally explained by advection of warmer water from remote locations and by regional changes in Ekman downwelling and in the ice-shelf melt-induced circulation, while increased iceberg melt plays no significant role. Our simulations suggest that high-end melt projections previously used to constrain recent sea level projections may have been significantly overestimated.

Plain Language Summary

Future sea level rise highly depends on how fast the ocean will melt the floating ice shelves in Antarctica, which modulates the ice flow from the ice sheet into the ocean. This is particularly true for the Amundsen Sea sector where the ice flow into the ocean is very sensitive to ocean-induced melting. Here we use a numerical model that represents the evolution of the Amundsen Sea, including under the floating ice shelves. Under a high-end greenhouse-gases concentration pathway, our simulations indicate that melt rates beneath the ice shelves may increase by 40 to 120%. This is explained by both warmer seawater coming from distant regions and changes in the local wind stress. Our simulations suggest that high-end melt projections previously used to constrain recent sea level projections may have been overestimated.

1 Introduction

Most projections of the Antarctic contribution to sea level rise are based on standalone ice sheet models in which melting beneath ice shelves is parameterized (Levermann et al., 2020; Seroussi et al., 2020; DeConto et al., 2021; Edwards et al., 2021). The existing melt parameterizations are based on highly simplified representations of the ocean circulation and heat exchanges in ice shelf cavities, and the resulting melt rates are significantly biased (Favier et al., 2019; Burgard et al., 2022). Furthermore, these melt parameterizations are typically driven by ocean warming derived from simulations of the Climate Model Intercomparison Project (CMIP, Eyring et al., 2016), although ice shelf cavities are not represented and ocean properties on the Antarctic continental shelf are significantly biased (Purich & England, 2021).

To either trust or challenge these ice sheet and sea level projections, our community needs projections that resolve the ocean dynamics over the Antarctic continental shelf and beneath the ice shelves, but such projections are rare (Asay-Davis et al., 2017). Timmermann and Hellmer (2013) and Naughten et al. (2018) pioneered CMIP-based projections at the Antarctic scale, using a global ocean model with refined resolution around Antarctica and beneath ice shelves. Their projections were nonetheless of limited use for the Amundsen Sea sector because of a substantial cold bias in their present-day state. Siahaan et al. (2021) were the first to run a global climate model (i.e., land, ocean, atmosphere) with an interactive Antarctic Ice Sheet in scenario-based projections. Their present-day melt rates were reasonable in the Amundsen Sea, but they found little change in their projections and questioned the representation of the Amundsen cavities at their resolution (e.g., only 11 grid columns for Pine Island ice shelf cavity). Stronger present-day biases were nonetheless found at higher ocean resolution in their model configuration (Smith et al., 2021).

Given that the Antarctic Ice Sheet projections show the highest sensitivity to increased basal melting in the Amundsen Sea sector (together with the Wilkes Land sector, Seroussi et al., 2020), it seems crucial to better estimate possible future ice shelf melt rates in that region and describe the associated mechanisms. Recent simulations of the Amundsen Sea by Naughten et al. (2022) have shown that relatively warm periods become more dominant over the 20$^{\text{th}}$ century, causing stronger ice shelf melting. In this paper, we use a regional ocean–sea-ice–ice-shelf model to build new projections to 2100 under the RCP8.5 scenario for the Amundsen Sea region and to describe the mechanisms explaining changes in ice shelf melt rates. High-end sea level projections projections are needed from an adaptation perspective (Hinkel et al., 2019; Durand et al., 2022), but are currently extremely uncertain, partly due to the poorly constrained sensitivity of ice shelf melt rates to ocean warming (Fox-Kemper et al., 2021; Edwards et al., 2021). This is our motivation to focus on the RCP8.5 scenario, which is on the higher end of possible scenarios in a world with no climate policy (Hausfather & Peters, 2020a, 2020b). Finally, we use our ocean projections to assess existing melt parameterizations recently used in ice sheet projections.

2 Ocean–sea-ice–ice-shelf simulations

We make use of the NEMO-3.6 (Nucleus for European Modelling of the Ocean, Madec & NEMO-team, 2016) ocean model that includes the LIM3 (Louvain Ice Model, Rousset et al., 2015) sea ice model and the ice shelf cavity module developed by Mathiot et al. (2017). The grid extends from 142.1°W to 84.9°W and from 76.5°S to 59.7°S, and has a resolution of 1/12° in longitude, i.e., a quasi-isotropic resolution varying from 4.7 km at the northern boundary to 2.2 km in the southernmost part of the domain. We use 75 vertical levels of thickness ranging from 1 m at the surface to 204 m at 6000 m depth, and a typical thickness of 30 to 100 m for ocean cells beneath ice shelves. Unless stated otherwise, the parameters are those used in Jourdain et al. (2017) and the complete set of NEMO parameters is provided on `https://doi.org/10.5281/zenodo.6644859`.

To get a rough estimate of the model uncertainty, we run an ensemble of three present-day and future simulations. For ensemble member A, the ice shelf and seabed topography is extracted from BedMachine-Antarctica-v1.33 (Morlighem et al., 2020), while members B and C are based on BedMachine-Antarctica-v2.0 (Morlighem, 2020). Additionally, B and C include a representation of grounded tabular icebergs, in particular B22A (Antarctic Iceberg Tracking Database, Budge & Long, 2018), whose ungrounded parts are treated as an ice shelf, and the line of icebergs grounded on Bear Ridge (Nakayama et al., 2014; Bett et al., 2020). The ocean–ice-shelf heat exchange coefficient (Γ_T) is 2.21×10^{-2} in A vs 1.88×10^{-2} in B-C, while the ocean–ice-shelf salt exchange coefficient is always defined as $\Gamma_S = \Gamma_T/35$. Finally, two parameters of the sea ice model differ: the maximum permitted sea ice concentration is set to 99.9% of the mesh in A-B vs 95% in C, and the ice–ocean drag coefficient is set to 5.0×10^{-3} in A-B vs 2.5×10^{-3} in C. All these parameter values are commonly used in the NEMO community. Our ensemble is designed to simply illustrate the importance of a few empirical choices and cannot be considered as a deep exploration of NEMO's parametric uncertainty (e.g., Williamson et al., 2017).

Our present-day simulations cover 1989–2009, following 10 years of spin up from 1979. The surface boundary conditions consist of 3-hourly (temperature, humidity, wind velocity) and daily (radiative fluxes and precipitation) mean outputs of the 10 km MAR (Regional Atmospheric Model, Gallée & Schayes, 1994) configuration described and evaluated by Donat-Magnin et al. (2020). The lateral ocean and sea ice boundary conditions consist of 5-day mean outputs of a global 0.25° NEMO simulation very similar to the one described by Merino et al. (2018) except that it is spun up from 1958 and that the imposed ice shelf melt flux increases linearly from 1990 to 2005 and is constant before and after that, with values corresponding to the FRESH− and FRESH+ reconstructions of

Merino et al. (2018). The global 0.25° simulation represents Lagrangian icebergs (Merino et al., 2016), and their 5-day averaged melt rate (Jourdain, Merino, et al., 2019) is applied at the surface of our regional 1/12° configuration. In addition, seven tidal constituents are applied at the lateral boundaries as in (Jourdain, Molines, et al., 2019). Our present-day simulations are evaluated in sup. section S1. In summary, our simulations are too warm at depth by approximately 0.5°C, and ice shelf melt rates are consequently slightly overestimated.

Our future simulations cover 2080–2100 and are representative of the CMIP5 multi-model mean under the RCP8.5 concentration pathway. The surface boundary conditions are taken from the MAR regional projections described and evaluated through a perfect-model approach in Donat-Magnin et al. (2021). The atmospheric projections themselves were driven at their surface and lateral boundaries by the mean seasonal anomalies (2080–2100 minus 1989–2009) derived from 33 CMIP5 models under the RCP8.5 scenario (more details are provided in Donat-Magnin et al., 2021). Our future simulations start from the 1979 ocean conditions (same as present-day), and are spun up for 10 years under warm conditions using the same method as for 2080–2100. Due to its open lateral boundaries, our regional ocean model configuration is no longer sensitive to its initial state after approximately seven years (Jourdain et al., 2017), which means that starting our future runs from the present-day conditions is acceptable as long as we allow some years for spin up, and it is not required to simulate the entire 2010–2070 period to estimate melt rates at the end of the 21st century.

The applied anomalies induce an eastward zonal wind and sea ice stress anomaly along the shelf break and offshore (Fig. 1a,b), which is a known response of the CMIP models to high greenhouse gases concentrations by 2100 (Swart & Fyfe, 2012; Holland et al., 2019; Goyal et al., 2021). We also find an increased westward stress along most of the ice sheet margin (Fig. 1b), which is possibly related to higher air temperature gradient across the ice-sheet–ocean boundary in the presence of reduced sea ice cover in the future. On average over the continental shelf, the Ekman downward velocity due to the wind and sea ice stress is weakened by 50% in the future compared to present day (sup. section S2).

In terms of surface heat fluxes, the Amundsen continental shelf loses 41% less energy to the atmosphere in the future compared to present-day (Fig. 1c,d), which is consistent with the effect of a warmer troposphere on downward sensible and longwave heat fluxes over the open ocean and sea ice. Precipitation increases by 22% (Fig. 1e,f) due to a higher water holding capacity of the troposphere in a warmer climate (Donat-Magnin et al., 2021). The increased precipitation and the reduced sea ice production over the continental shelf (from 0.23 to 0.19 $\mathrm{Gt\,yr^{-1}}$) are together responsible for an annual rate of surface buoyancy loss reduced by 75% in the future compared to present day (supp. section S2).

We adopt a similar approach for the lateral boundaries of our regional ocean–sea-ice simulations and add the CMIP5 multi-model mean seasonal anomalies to the present-day lateral boundary conditions (for temperature, salinity, ocean velocity, sea ice concentration, sea ice thickness, and snow-on-ice thickness). The perturbation applied at our lateral boundaries is comprehensively described in sup. section S3, which can be summarised as a warming that exceeds 0.25°C everywhere in the first 1000 m and reaches 2°C in the northernmost part of our domain, as well as a freshening of the first 100 m that is particularly pronounced near the Antarctic coast.

Two additional sensitivity experiments are performed for further insight into the processes. First, we repeat the future simulation of ensemble member B but we only apply the future surface forcing, i.e., we keep the present-day lateral boundary conditions for ocean and sea ice. Second, we repeat the future simulation of ensemble member C but with increased iceberg melting (which is kept at present-day values in the other ex-

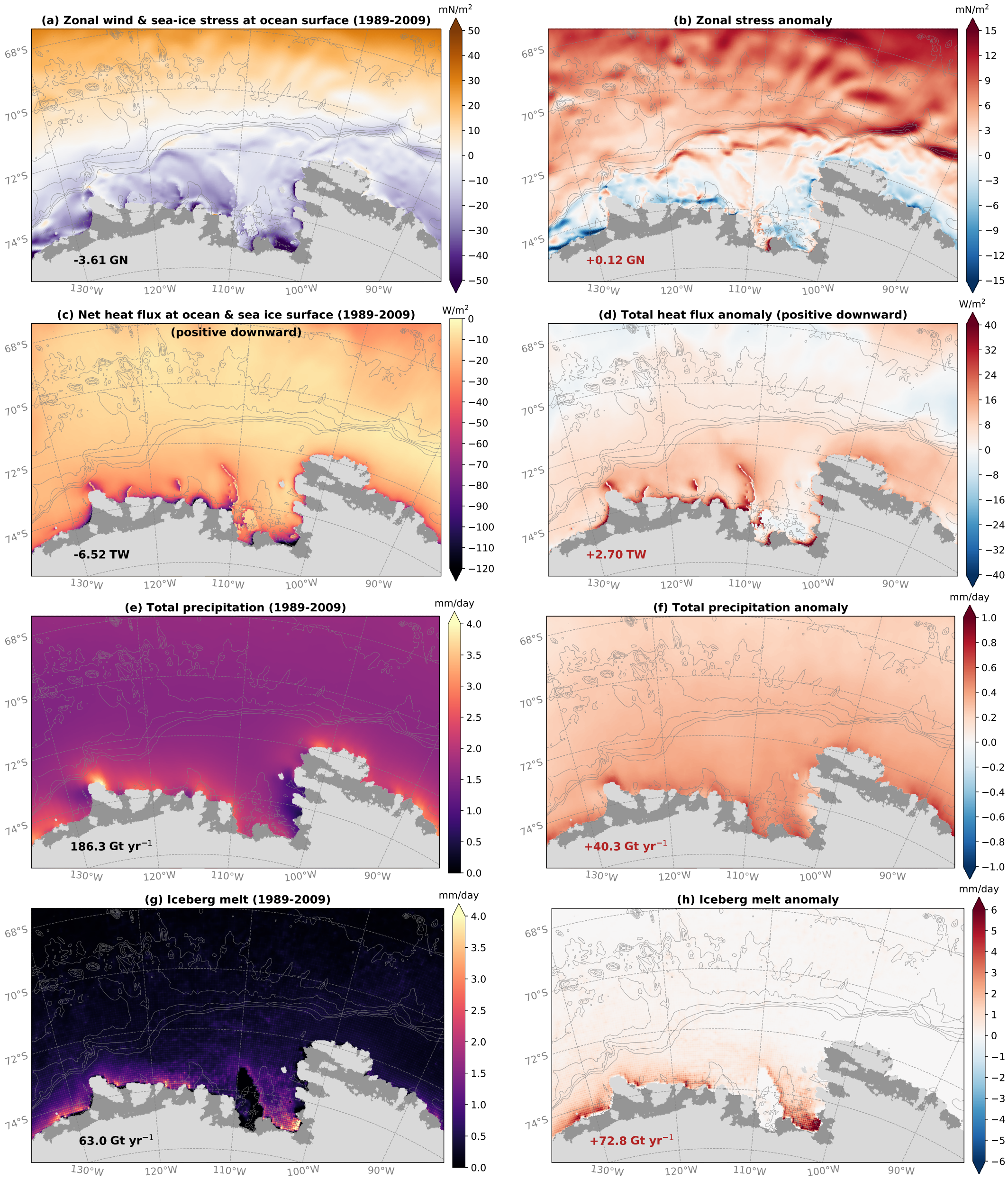

Figure 1. Present-day atmospheric forcing (left) and future anomalies with respect to present day (right). Anomalies are calculated as the average of 2080–2100 minus 1989–2009. The grounded ice sheet and the ice shelves are shaded in light and dark grey, respectively. The grey contours indicate the bathymetry (every 750 m). Numbers near the lower left corner indicate the value of the plotted field integrated over the continental shelf, which is defined as the area between the 1500 m isobath and the coastline, and between 100°W and 135°W.

periments). Following the calculations presented in section S4, we increase the total iceberg melt flux over the Amundsen continental shelf from 63 $\mathrm{Gt\,yr^{-1}}$ at present-day to 136 $\mathrm{Gt\,yr^{-1}}$ at the end of the 21st century under RCP8.5 (Fig. 1g,h).

3 Results: changes in ice shelf basal melting and related processes

On average over the three ensemble members, the ice shelf melt rates are multiplied by 1.4 to 2.2 (depending on the ice shelf) from present day to future (Fig. 2a). The total ice shelf meltwater flux in the Amundsen Sea increases by 347 $\mathrm{Gt\,yr^{-1}}$ on average (Fig. 2b,c), with a standard deviation of 54 $\mathrm{Gt\,yr^{-1}}$ across the ensemble.

Interestingly, members B and C give almost identical future melt rates while present-day values differ significantly (Fig. 2a). As the only difference between B and C is the set of sea ice parameters, this indicates that sea ice production and the related surface buoyancy flux are important drivers of ice shelf melting presently, but no longer play a role in the future. This is very likely related to both the 75% reduction of the surface buoyancy loss in the future and the mixing of more ice shelf meltwater into the surface layer. Both increase the ocean stratification and prevent surface waters from reaching deeper warmer layers on the continental shelf through convective mixing. We also do not find any significant difference between projection C with and without increased iceberg melt rates (not shown), which supports the idea of a decoupling between the surface and the deeper layers in the future.

The changes in melt rates for member B without perturbations of NEMO's lateral boundaries are shown by the white disruption of the middle brown bars in Fig. 2a. Increased melt rates underneath Abbot and Venable ice shelves are almost entirely explained by the modified lateral boundary conditions. For the other ice shelves, the part of increased melt rate attributed to the lateral boundaries varies from 1/3 to 2/3 of the total change, depending on the ice shelf. This indicates that future changes in remote ocean properties are important, i.e., local changes in the atmospheric forcing cannot entirely explain the projected increase in ice shelf melt rates.

We then use the terms of the exact heat and salt budget (saved online and calculated as in Jourdain et al., 2017) to get further insights into the physical mechanisms. The offshore projection is characterised by a 0.25°C warming below the thermocline due to horizontal advection from the domain boundaries, a 75 m higher thermocline explained by horizontal advection and decreased convective mixing due to less sea ice formation, and a surface freshened by 0.4 $\mathrm{g\,kg^{-1}}$ (Fig. S6 and its description in sup. section S4). Changes over the continental shelf are more intense, with 0.5°C warming at depth, a 160 m higher thermocline (Fig. 3a), and surface freshened by 0.5 $\mathrm{g\,kg^{-1}}$ (Fig. 3b). In contrast to the offshore mechanisms, vertical advection plays a key role on the continental shelf (Fig. 3c,d). Approximately half of the heat brought by changes in vertical advection between 250 and 800 m is due to the melt-induced circulation in ice shelf cavities and is mostly consumed as latent heat for ice melting (compare Fig. 3c,d to Fig. 3e,f). The remaining part is consistent with the reduced Ekman downwelling described in the previous section and in Spence et al. (2014) and Naughten et al. (2022), which reduces the downward advection of relatively cold and fresh water from the surface layer (above 250 m) to deeper layers (Fig. 3c,d). A closer look at the budget terms within ice shelf cavities (not shown) reveals an additional input of heat and freshwater between 100 and 400 m depth corresponding to the melt-induced circulation that releases a mixture of meltwater and entrained Circumpolar Deep Water (CDW) at the ice shelf front as described by Jourdain et al. (2017).

The strong freshening of the surface layer (above 250 m) is dominated by increased ice shelf melting. Out of the 347 $\mathrm{Gt\,yr^{-1}}$ of additional ice shelf meltwater, only 51 $\mathrm{Gt\,yr^{-1}}$ are injected directly into the surface layer, but the absence of sub-surface freshening (Fig. 3b)

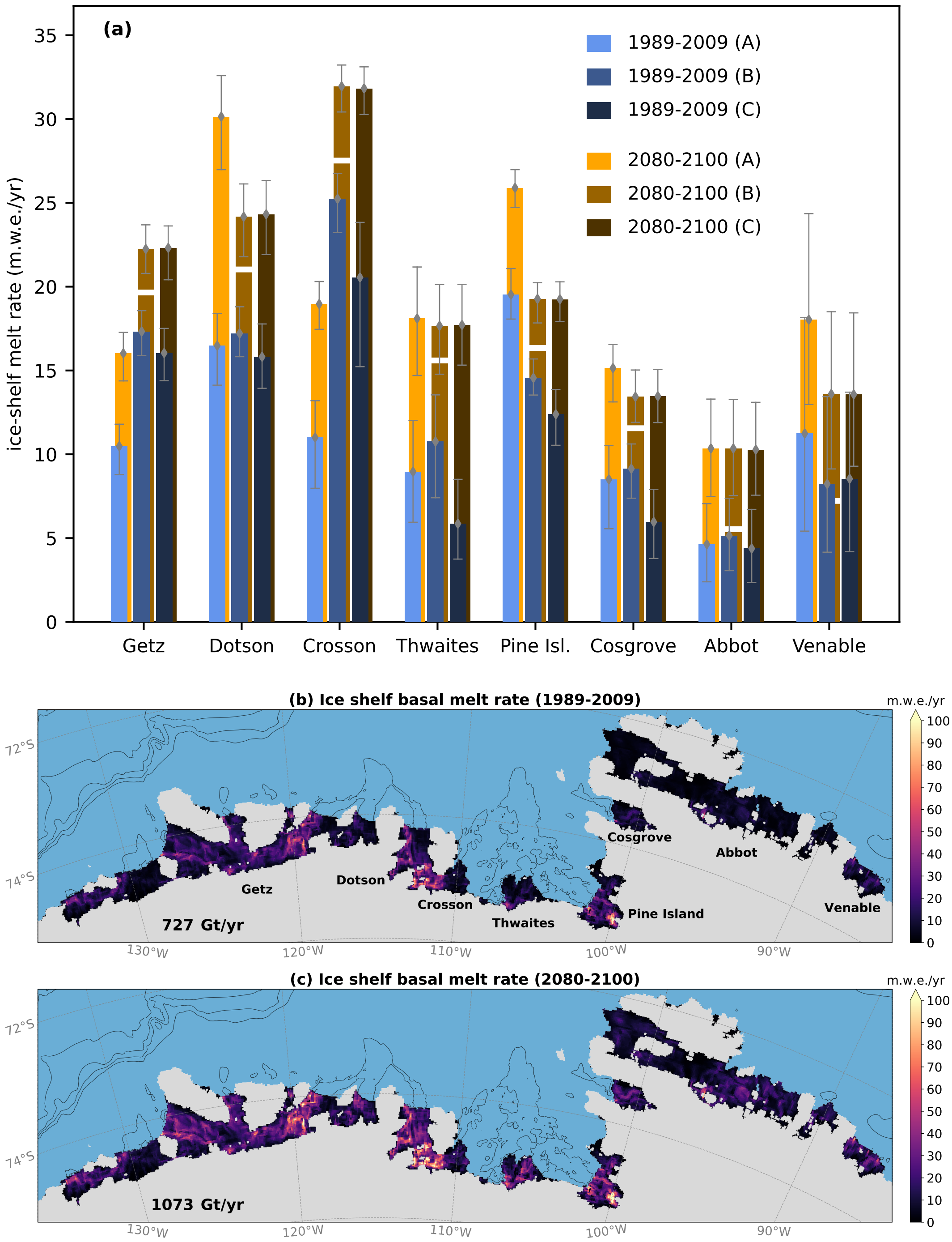

Figure 2. (a) Mean present day and future melt rates of individual ice shelves in model configurations A, B and C (in meters of liquid water equivalent per year, i.e. 10^3 kg m^{-2} yr^{-1}). The grey bars cover 95% of the monthly values, i.e. between the 2.5$^{\text{th}}$ and the 97.5$^{\text{th}}$ percentiles. The white disruption of the light brown bars (B over 2080-2100) represent the future melt rate in the experiment with lateral boundary conditions kept at present-day values. (b,c) Present-day and future ice shelf melt rates, and integrated value over the domain in the lower left corner. The black contours indicate the bathymetry (every 750 m).

and the examination of the role of vertical advection in Fig. 3d,f indicate that most of the additional ice shelf meltwater is transported towards the surface layer. These additional 347 $\mathrm{Gt\,yr^{-1}}$ are much larger than the 73 $\mathrm{Gt\,yr^{-1}}$ of increased iceberg melting (Fig. 1h), 40 $\mathrm{Gt\,yr^{-1}}$ of increased precipitation (Fig. 1f), and a sea ice production decreased by 37 $\mathrm{Gt\,yr^{-1}}$ which is equivalent to a freshwater release of 30 $\mathrm{Gt\,yr^{-1}}$ (for a sea ice salinity of 6.3 $\mathrm{g\,kg^{-1}}$).

4 Results: assessment of simple ice shelf melt parameterizations

Here we use our NEMO projections to assess the non-local (also referred to as semi-local) quadratic parameterization proposed by Favier et al. (2019) and used in some of the standard ice sheet projections of the Ice Sheet Model Intercomparisaon Project for CMIP6 (ISMIP6, Nowicki et al., 2020; Seroussi et al., 2020), with a melt rate defined as:

$$m(x,y) = K \times (TF(x,y,z_{\text{draft}}) + \delta T) \times |\langle TF \rangle_{\text{ice-shelf}} + \delta T| \tag{1}$$

where $TF(x,y,z_{\text{draft}})$ is the thermal forcing at the ice-ocean interface of depth z_{draft}, and $\langle TF \rangle_{\text{ice-shelf}}$ the thermal forcing averaged over an entire ice shelf draft. The temperature correction δT is used to correct biases in present-day observations and to account for melt-induced cooling or other poorly represented processes (Jourdain et al., 2020). K is a tuning coefficient that was expressed in various ways across previous studies. An expression of K was proposed by Favier et al. (2019) and Jourdain et al. (2020), but we find the expression proposed by Jenkins et al. (2018) and Burgard et al. (2022) more physically sound. For ISMIP6, Jourdain et al. (2020) proposed two calibration methods, one referred to as "MeanAnt", ensuring realistic present-day melt rates at the scale of Antarctica for minimal temperature corrections and giving $K_{\text{MeanAnt}} = 2.57\ \mathrm{m\,yr^{-1}\,K^{-2}}$, and the other one referred to as "PIGL", ensuring more realistic present-day melt rates near Pine Island's grounding line and giving $K_{\text{PIGL}} = 28.2\ \mathrm{m\,yr^{-1}\,K^{-2}}$, but requiring negative δT corrections almost everywhere to keep reasonable melt rates for individual ice shelves or integrated over larger sectors.

In the following, we assume that the present-day temperature is perfectly known, so that we can use $\delta T = 0$ for MeanAnt and we find that present-day RMSE from PIGL are lowest for $\delta T = -1.9$°C. For clarity, we just show the results for Pine Island and Thwaites (Fig. 4), which are key ice shelves for the Antarctic contribution to sea level rise, but the other ice shelves have a very similar behaviour. We estimate the future parameterized melt rates in two ways: (1) from the future ocean temperatures simulated by NEMO (orange dashed curves in Fig. 4), and (2) from the CMIP5 multi-model mean ocean warming added to the NEMO present-day temperatures (dashed dark red curves in Fig. 4) which corresponds to what is commonly used in standalone ice sheet projections like ISMIP6.

First of all, the present-day parameterized melt rates overall agree with NEMO although the exact vertical distribution is only poorly captured (blue curves in Fig. 4). The MeanAnt curves show some overlap between the three model projections and the 90$^{\text{th}}$ confidence interval of the parameterized projections (orange curves in Fig. 4a,b), although the RMSE approximately doubles compared to present day. The PIGL projections are much worse, with very little overlap between the three model projections and the 90$^{\text{th}}$ confidence interval of the parameterized projections (orange curves in Fig. 4c,d). For the 95$^{\text{th}}$ percentile of K, the maximum melt rates in either Pine Island or Thwaites cavity are overestimated by a factor of five. The melt projections directly based on the CMIP5 ocean warming (dashed dark red curves in Fig. 4) are similar to the projections from the warming produced by NEMO, indicating that most of the bias comes from the parameterization itself.

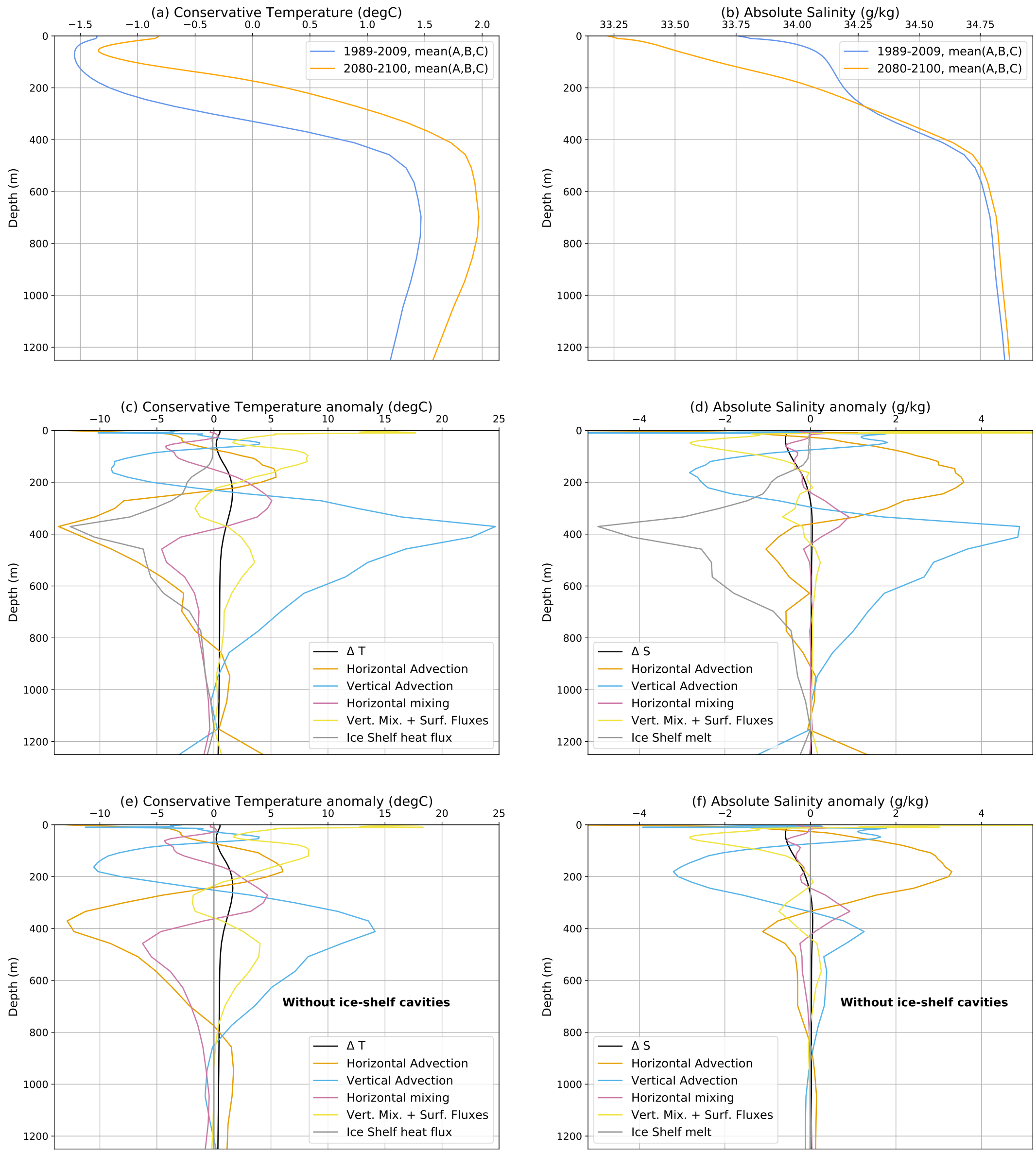

Figure 3. (a,b) Present-day and future conservative temperature and absolute salinity profiles over the Amundsen Sea continental shelf (defined as the area between the 1500 m isobath and the coastline, and between 100°W and 135°W), including ice shelf cavities. (c,d) temperature (ΔT) and salinity (ΔS) change from present-day to future conditions and contributions of the individual terms of the heat and salt equations to ΔT and ΔS, respectively. The individual tendency terms of the heat and salt equations were integrated in time from the initial state until each month of either 1989-2009 or 2080-2100, then averaged over each of these 20-year period, from which we extracted the difference between the two periods (similar to equations 6 and 7 of Jourdain et al., 2017). (e,f) same as (c,d) but excluding ice shelf cavities from the heat and salt budget calculation.

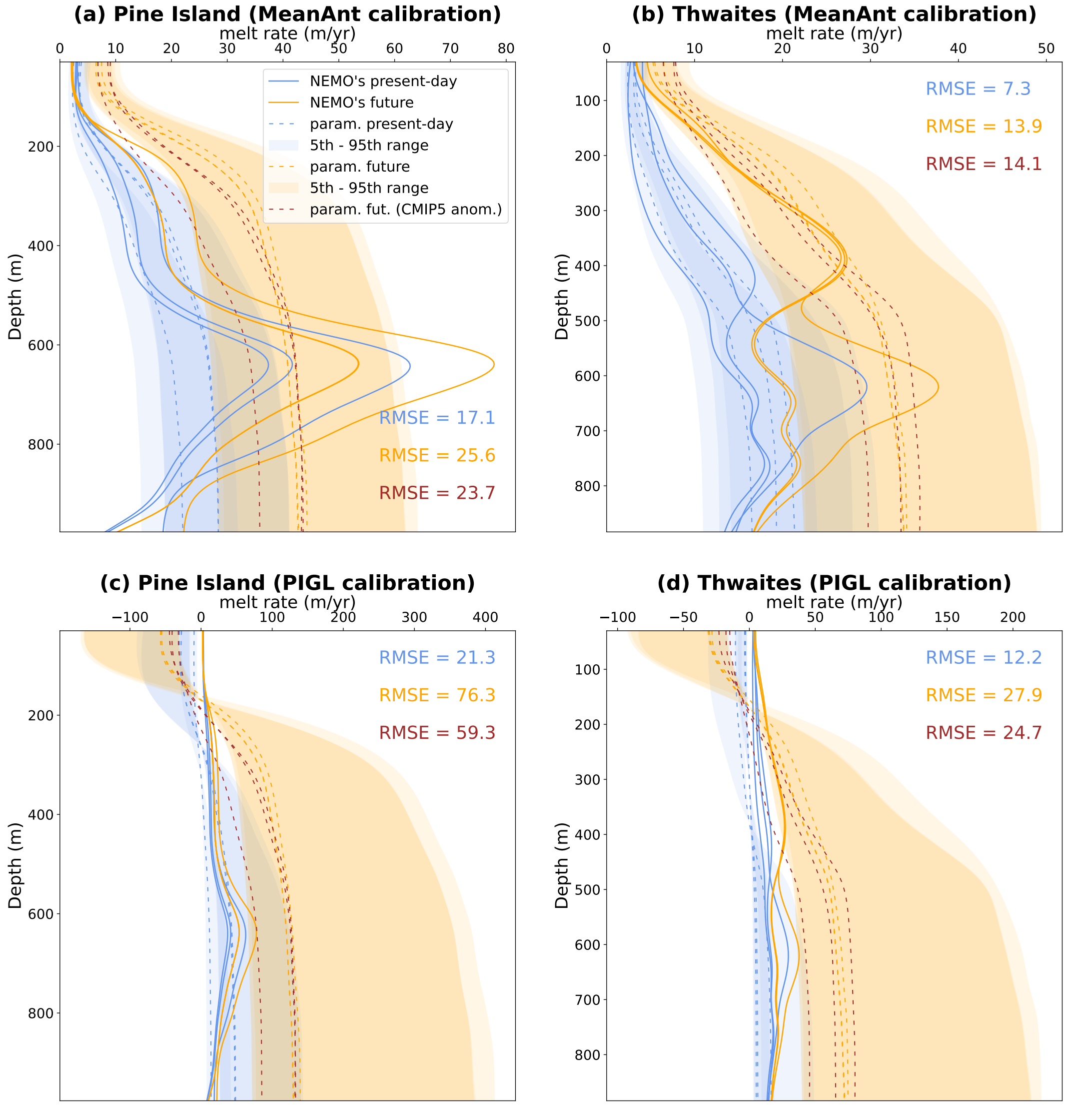

Figure 4. Melt profiles beneath Pine Island (left) and Thwaites (right) ice shelves, from the NEMO simulations (solid lines), and from the ISMIP6 standard parameterization (dashed lines) tuned following either the "MeanAnt" (upper panels) or the "PIGL" (lower panels) method (median K coefficient derived from Jourdain et al., 2020). The present day parameterized melt rates are based on NEMO's present-day temperatures in front of the ice shelf cavities (within 50 km from the ice shelf front). The future melt rate is either calculated from the's future temperatures simulated by NEMO (orange dashed lines) or from the CMIP5 multi-model mean temperature anomaly (dark red dashed lines). The semi-transparent shaded areas indicate the range corresponding to the 5^{th} and 95^{th} percentiles of K coefficients based on the future temperatures produced by NEMO (values derived from Tab. 2 of Jourdain et al. 2020). The three curves for each estimate correspond to the three members of our small ensemble. Every curve is built using a kernel density estimate based on a Gaussian function of standard deviation equal to $1/20^{\mathrm{th}}$ of the maximum ice draft depth. The Root Mean Square Errors (RMSE, in m/yr) are calculated for the spatial pattern with regards to the NEMO values and correspond to the median K values.

5 Discussion and conclusion

In this paper, we have built an ensemble of three 1/12° ocean–sea-ice–ice-shelf projections of the late 21st century under the RCP8.5 concentration pathway. In these simulations, the net surface buoyancy loss is reduced by 75% in the future compared to present day due to surface freshening by increased precipitation, increased iceberg melt and reduced sea ice production. Increased ice shelf melt also contributes greatly to making the surface layer fresher and more buoyant in the future. The result is a decoupling between the surface layer and deeper layers on the continental shelf, which makes future ice shelf melt insensitive to additional perturbations of surface buoyancy fluxes. We find that the future Ekman downwelling velocity is reduced by half over the continental shelf compared to present day. This, in addition to the melt-induced circulation, largely explains the additional heat made available to ice shelf melting. However, regional changes in atmospheric forcing only explain 1/3 to 2/3 of the increase in ice shelf melt rates (depending on the ice shelf). The remaining is due to advection of warmer water from remote locations (i.e. from our model domain lateral boundaries). The importance of advection from remote locations was already evidenced by Nakayama et al. (2018) for the interannual variability of the Amundsen Sea. Here we clearly show the caveats of attributing future changes in ice shelf melting to regional atmospheric perturbations in the Amundsen Sea (e.g., Holland et al., 2019).

The relative changes in melt rates (+48% for all simulated ice shelves, Fig. 2b,c) are lower than previous estimates, e.g., +189% until 2100 in the Amundsen Sea for the CMIP5 multi-model mean under RCP8.5 in Naughten et al. (2018) and +250% until 2100 for Pine Island under the A1B and E1 scenarios in Timmermann and Hellmer (2013). The present-day melt rates were strongly underestimated in these previous studies, due to a cold bias that suggests overestimated deep convection related to overestimated sea ice production and/or too weak vertical density stratification (e.g. from underestimated precipitation). Such a cold Amundsen Sea is therefore very sensitive to changes in surface heat and buoyancy fluxes that can induce a transition from sea-floor temperatures near the surface freezing point to much warmer conditions typical of the presence of CDW. In our case, we start from a more realistic state with weakly modified CDW on the continental shelf, so that important warming at depth cannot be triggered by surface heat and buoyancy fluxes, and the Ekman dynamics is the main driver of changes in ice shelf melt rates. We nonetheless acknowledge that our 0.5°C warm bias may lead to an underestimation of present-day episodic convection, leading to an underestimation of the ocean warming and relative increase in ice shelf melt rates. For a given ocean warming, starting from cold biased conditions also produces important relative changes in melt rates because the calculation of relative change involves a division by the initial thermal forcing. For example, assuming a quadratic dependency of melt to the thermal forcing (Holland et al., 2008), 0.5°C of future warming at 600 m depth would correspond to melt rates increased by 143% starting from the -2.6°C bias of Naughten et al. (2018), by 30% starting from an observed temperature of 1.0°C (Dutrieux et al., 2014) and by 26% (starting from our simulations with a +0.5°C bias).

Our projection method is innovative in the sense that it enables a representation of the CMIP multi-model mean at relatively high resolution and with basic bias correction. We have chosen to drive our projections directly by the CMIP multi-model mean because it is often considered as the best estimate for future climate as individual model biases are partly cancelled (Knutti et al., 2010). The use of future anomalies with respect to present day is expected to remove a part of the biases in individual model projections given that the CMIP model biases are largely stationary even under strong climate changes (Krinner & Flanner, 2018), while conserving linearities like the geostrophic balance. Besides, the numerical cost of each 1/12° ocean simulation precludes forcing them by each of the 33 CMIP5 models for both present and future conditions. However, an important limitation of our projection method is that we do not account for possible changes in the frequency of interannual events like El Niño (Cai et al., 2014), and it will be important to confront our results to direct downscaling of the CMIP models. Finally, we have chosen to force our ocean simulations using a 10 km regional atmospheric model, which is expected to be more realistic along the coastline and the shelf break than the much coarser CMIP models (e.g., Dinniman et al., 2015; Huot et al., 2021), although the use of such an intermediate model may be an additional source of biases and uncertainty in the chain of projections. The regional atmosphere model (MAR) is nonetheless renowned for its representation of polar processes in the Antarctic coastal region (e.g., Donat-Magnin et al., 2020; Mottram et al., 2021; Kittel et al., 2022), while most CMIP models have representations of snow, clouds and surface boundary layers that are less accurate in polar regions (e.g., Lenaerts et al., 2016, 2017). Yet, it will be important to explore other projection methods to confirm the results of this study.

All our conclusions are nonetheless based on a single ocean model, even if we used three different set-ups, and it will be important to challenge these results using different ocean models. Our 1/12° resolution enables the resolution of eddies in the Southern Ocean, which is key to simulating future sea ice decline (Rackow et al., 2022) and future heat transport towards Antarctica (van Westen & Dijkstra, 2021). This resolution is also sufficient for the resolution of mean flow topography interactions involved in bringing CDW onto the continental shelf (St-Laurent et al., 2013), but not sufficient to resolve eddies on the continental shelf and within ice shelf cavities (Stewart et al., 2018, e.g.,), or the interaction between Rossby waves along the shelf break and bathymetric troughs (St-Laurent et al., 2013). It remains difficult to estimate the role of these small scales on the evolution of heat transport towards the ice shelf cavities of the Amundsen Sea as previous high-resolution studies did not represent fine-scale bathymetry and ice shelf cavities in the Amundsen Sea (Stewart et al., 2018). Another important limitation of our modelling approach is that there is no ice sheet model coupled to NEMO in this study, i.e., ice shelves are static. This was shown to be an important limitation (Donat-Magnin et al., 2017), albeit for much stronger and longer melt perturbations.

Finally, given that the Antarctic Ice Sheet projections show the highest sensitivity to increased basal melt rates in the Amundsen Sea sector (Seroussi et al., 2020), our regional results can provide a critical perspective on the Antarctic contribution to the 21$^{\text{st}}$ century sea level rise simulated within ISMIP6 (Seroussi et al., 2020) and emulated by Edwards et al. (2021). The high-end estimates for 2100 under RCP8.5 ($\sim$30 cm of additional sea level) were obtained from the 95$^{\text{th}}$ percentile of the PIGL parameters, which we find highly incompatible with our simulations. Edwards et al. (2021) empirically defined a continuous distribution of K coefficients (their Fig. 3d), with a relatively large cumulative probability around the median PIGL parameter, and low-probability extreme values beyond the 95$^{\text{th}}$ percentile of PIGL parameters. Our projections suggest that this distribution should be narrowed towards lower values and that lower parameters should be used even for risk averse projections.

Data and softwares

The model version and set of parameters used to run our experiments are provided in `https://doi.org/10.5281/zenodo.6644859`. All the python scripts used to build the figures are provided in `http://github.com/nicojourdain/SCRIPTS_PAPER_PLOTS` and are mainly based on the Xarray (Hoyer & Hamman, 2017), Numpy (Harris et al., 2020) and Matplotlib (Hunter, 2007) packages. THE GITHUB REPOSITORIES WILL BE ARCHIVED ON `http://zenodo.org` AFTER ACCEPTANCE.

Acknowledgments
This publication is PROTECT contribution number XX. This study was funded by the European Union's Horizon 2020 research and innovation programme under grant agree-

ments No 869304 (PROTECT), No 820575 (TiPACCs) and No 101003826 (CRiceS). It was also partly funded by the French National Research Agency under grant No ANR-19-CE01-0015 (EIS). This work was granted access to the HPC resources of CINES under the allocation A0100106035 attributed by GENCI.

References

Asay-Davis, X. S., Jourdain, N. C., & Nakayama, Y. (2017). Developments in Simulating and Parameterizing Interactions Between the Southern Ocean and the Antarctic Ice Sheet. *Current Climate Change Reports*, *3*(4), 316–329.

Bett, D. T., Holland, P. R., Naveira Garabato, A. C., Jenkins, A., Dutrieux, P., Kimura, S., & Fleming, A. (2020). The impact of the Amundsen Sea freshwater balance on ocean melting of the West Antarctic Ice Sheet. *J. Geophys. Res. Oceans*, *125*(9), e2020JC016305.

Budge, J. S., & Long, D. G. (2018). A comprehensive database for Antarctic iceberg tracking using scatterometer data. *IEEE Journal of Selected Topics in Applied Earth Observations and Remote Sensing*, *11*(2), 434–442.

Burgard, C., Jourdain, N. C., Reese, R., Jenkins, A., & Mathiot, P. (2022). An assessment of basal melt parameterisations for Antarctic ice shelves. *The Cryosphere Discussion*, *0*, 0–0.

Cai, W., Borlace, S., Lengaigne, M., Van Rensch, P., Collins, M., Vecchi, G., … others (2014). Increasing frequency of extreme El Niño events due to greenhouse warming. *Nat. Clim. Change*, *4*(2), 111–116.

DeConto, R. M., Pollard, D., Alley, R. B., Velicogna, I., Gasson, E., Gomez, N., … others (2021). The Paris Climate Agreement and future sea-level rise from Antarctica. *Nature*, *593*(7857), 83–89.

Dinniman, M. S., Klinck, J. M., Bai, L.-S., Bromwich, D. H., Hines, K. M., & Holland, D. M. (2015). The Effect of Atmospheric Forcing Resolution on Delivery of Ocean Heat to the Antarctic Floating Ice Shelves. *J. Climate*, *28*(15), 6067–6085.

Donat-Magnin, M., Jourdain, N. C., Gallée, H., Amory, C., Kittel, C., Fettweis, X., … Agosta, C. (2020). Interannual Variability of Summer Surface Mass Balance and Surface Melting in the Amundsen Sector, West Antarctica. *The Cryosphere*, *14*(1), 229–249.

Donat-Magnin, M., Jourdain, N. C., Kittel, C., Agosta, C., Amory, C., Gallée, H., … Chekki, M. (2021). Future surface mass balance and surface melt in the Amundsen sector of the West Antarctic Ice Sheet. *The Cryosphere*, *15*(2), 571–593.

Donat-Magnin, M., Jourdain, N. C., Spence, P., Le Sommer, J., Gallée, H., & Durand, G. (2017). Ice-Shelf Melt Response to Changing Winds and Glacier Dynamics in the Amundsen Sea Sector, Antarctica. *J. Geophys. Res.*, *122*(12), 10206–10224.

Durand, G., van den Broeke, M. R., Le Cozannet, G., Edwards, T. L., Holland, P. R., Jourdain, N. C., … others (2022). Sea-level rise: From global perspectives to local services. *Frontiers in marine science*, 2088.

Dutrieux, P., De Rydt, J., Jenkins, A., Holland, P. R., Ha, H. K., Lee, S. H., … Schröder, M. (2014). Strong sensitivity of Pine Island ice-shelf melting to climatic variability. *Science*, *343*(6167), 174–178.

Edwards, T. L., Nowicki, S., Marzeion, B., Hock, R., Goelzer, H., Seroussi, H., … others (2021). Projected land ice contributions to twenty-first-century sea level rise. *Nature*, *593*(7857), 74–82.

Eyring, V., Bony, S., Meehl, G. A., Senior, C. A., Stevens, B., Stouffer, R. J., & Taylor, K. E. (2016). Overview of the Coupled Model Intercomparison Project Phase 6 (CMIP6) experimental design and organization. *Geosci. Model Dev.*, *9*(5), 1937–1958.

Favier, L., Jourdain, N. C., Jenkins, A., Merino, N., Durand, G., Gagliardini, O., . . . Mathiot, P. (2019). Assessment of Sub-Shelf Melting Parameterisations Using the Ocean-Ice Sheet Coupled Model NEMO (v3. 6)-Elmer/Ice (v8. 3). *Geosci. Model Dev.*.

Fox-Kemper, B., Hewitt, H., Xiao, C., Aalgeirsdóttir, G., Drijfhout, S. S., Edwards, T. L., . . . Yu, Y. (2021). Ocean, Cryosphere and Sea Level Change. In *Climate Change 2021: The Physical Science Basis. Contribution of Working Group I to the Sixth Assessment Report of the Intergovernmental Panel on Climate Change* (pp. 1211–1362). Cambridge University Press, Cambridge, United Kingdom and New York, NY, USA. doi: 10.1017/9781009157896.011

Gallée, H., & Schayes, G. (1994). Development of a three-dimensional meso-γ primitive equation model: katabatic winds simulation in the area of Terra Nova Bay, Antarctica. *Monthly Wea. Rev.*, *122*(4), 671–685.

Goyal, R., Sen Gupta, A., Jucker, M., & England, M. H. (2021). Historical and projected changes in the southern hemisphere surface westerlies. *Geophys. Res. Lett.*, *48*(4), e2020GL090849.

Harris, C. R., Millman, K. J., van der Walt, S. J., Gommers, R., Virtanen, P., Cournapeau, D., . . . others (2020). Array programming with NumPy. *Nature*, *585*(7825), 357–362. Retrieved from `https://doi.org/10.1038/s41586-020-2649-2` doi: 10.1038/s41586-020-2649-2

Hausfather, Z., & Peters, G. P. (2020a). Emissions-thebusiness as usual'story is misleading. *Nature*, *577*(7792), 618–620.

Hausfather, Z., & Peters, G. P. (2020b). RCP8. 5 is a problematic scenario for near-term emissions. *Proc. Natl. Acad. Sci. U.S.A.*, *117*(45), 27791–27792.

Hinkel, J., Church, J. A., Gregory, J. M., Lambert, E., Le Cozannet, G., Lowe, J., . . . van de Wal, R. (2019). Meeting user needs for sea level rise information: a decision analysis perspective. *Earth's Future*, *7*(3), 320–337.

Holland, P. R., Bracegirdle, T. J., Dutrieux, P., Jenkins, A., & Steig, E. J. (2019). West Antarctic ice loss influenced by internal climate variability and anthropogenic forcing. *Nature Geoscience*, 1–7.

Holland, P. R., Jenkins, A., & Holland, D. M. (2008). The response of ice shelf basal melting to variations in ocean temperature. *J. Climate*, *21*(11), 2558–2572.

Hoyer, S., & Hamman, J. (2017). xarray: N-D labeled arrays and datasets in Python. *J. Open Res. Softw.*, *5*(1). Retrieved from `https://doi.org/10.5334/jors.148` doi: 10.5334/jors.148

Hunter, J. D. (2007). Matplotlib: A 2D graphics environment. *Computing in Science & Engineering*, *9*(3), 90–95. doi: 10.1109/MCSE.2007.55

Huot, P.-V., Kittel, C., Fichefet, T., Jourdain, N. C., Sterlin, J., & Fettweis, X. (2021). Effects of the atmospheric forcing resolution on simulated sea ice and polynyas off Adélie Land, East Antarctica. *Ocean Modelling*, *168*, 101901.

Jenkins, A., Shoosmith, D., Dutrieux, P., Jacobs, S., Kim, T. W., Lee, S. H., . . . Stammerjohn, S. (2018). West Antarctic Ice Sheet retreat in the Amundsen Sea driven by decadal oceanic variability. *Nature Geosc.*, *11*, 733–738.

Jourdain, N. C., Asay-Davis, X., Hattermann, T., Straneo, F., Seroussi, H., Little, C. M., & Nowicki, S. (2020). A protocol for calculating basal melt rates in the ISMIP6 Antarctic ice sheet projections. *The Cryosphere*, *14*(9), 3111–3134.

Jourdain, N. C., Mathiot, P., Merino, N., Durand, G., Le Sommer, J., Spence, P., . . . Madec, G. (2017). Ocean circulation and sea-ice thinning induced by melting ice shelves in the Amundsen Sea. *J. Geophys. Res. Oceans*, *122*(3), 2550–2573.

Jourdain, N. C., Merino, N., Le Sommer, J., Durand, G., & Mathiot, P. (2019). *Interannual iceberg meltwater fluxes over the Southern Ocean (1.0)* (Tech. Rep.). Retrieved from `https://doi.org/10.5281/zenodo.3514728`

Jourdain, N. C., Molines, J.-M., Le Sommer, J., Mathiot, P., Chanut, J., de Lavergne, C., & Madec, G. (2019). Simulating or prescribing the influence of tides on the Amundsen Sea ice shelves. *Ocean Modelling*, *133*, 44–55.

Kittel, C., Amory, C., Hofer, S., Agosta, C., Jourdain, N. C., Gilbert, E., ... Fettweis, X. (2022). Clouds drive differences in future surface melt over the Antarctic ice shelves. *The Cryosphere*, *16*(7), 2655–2669.

Knutti, R., Furrer, R., Tebaldi, C., Cermak, J., & Meehl, G. A. (2010). Challenges in combining projections from multiple climate models. *J. Climate*, *23*(10), 2739–2758.

Krinner, G., & Flanner, M. G. (2018). Striking stationarity of large-scale climate model bias patterns under strong climate change. *Proceedings of the National Academy of Sciences*, *115*(38), 9462–9466.

Lenaerts, J. T. M., Van Tricht, K., Lhermitte, S., & L'Ecuyer, T. S. (2017). Polar clouds and radiation in satellite observations, reanalyses, and climate models. *Geophys. Res. Lett.*, *44*(7), 3355–3364.

Lenaerts, J. T. M., Vizcaino, M., Fyke, J., Van Kampenhout, L., & van den Broeke, M. R. (2016). Present-day and future Antarctic ice sheet climate and surface mass balance in the Community Earth System Model. *Clim. Dyn.*, *47*(5-6), 1367–1381.

Levermann, A., Winkelmann, R., Albrecht, T., Goelzer, H., Golledge, N. R., Greve, R., ... others (2020). Projecting Antarctica's contribution to future sea level rise from basal ice shelf melt using linear response functions of 16 ice sheet models (LARMIP-2). *Earth System Dynamics*, *11*(1), 35–76.

Madec, G., & NEMO-team. (2016). *NEMO ocean engine, version 3.6 stable, Note du Pôle de modélisation de l'Institut Pierre-Simon Laplace No 27, ISSN No 1288-1619* (Tech. Rep.). IPSL, France.

Mathiot, P., Jenkins, A., Harris, C., & Madec, G. (2017). Explicit and parametrised representation of under ice shelf seas in az* coordinate ocean model NEMO 3.6. *Geosci. Model Dev.*, *10*(7), 2849–2874.

Merino, N., Jourdain, N. C., Le Sommer, J., Goosse, H., Mathiot, P., & Durand, G. (2018). Impact of increasing antarctic glacial freshwater release on regional sea-ice cover in the Southern Ocean. *Ocean Model.*, *121*, 76–89.

Merino, N., Le Sommer, J., Durand, G., Jourdain, N. C., Madec, G., Mathiot, P., & Tournadre, J. (2016). Antarctic icebergs melt over the Southern Ocean : climatology and impact on sea-ice. *Ocean Model.*, *104*, 99–110.

Morlighem, M. (2020). *MEaSUREs BedMachine Antarctica, Version 2* (Tech. Rep.). Boulder, Colorado USA. NASA National Snow and Ice Data Center Distributed Active Archive Center. Retrieved from `https://nsidc.org/data/NSIDC-0756/versions/2` doi: 10.5067/E1QL9HFQ7A8M

Morlighem, M., Rignot, E., Binder, T., Blankenship, D., Drews, R., Eagles, G., ... others (2020). Deep glacial troughs and stabilizing ridges unveiled beneath the margins of the Antarctic ice sheet. *Nature Geoscience*, *13*(2), 132–137.

Mottram, R., Hansen, N., Kittel, C., van Wessem, J. M., Agosta, C., Amory, C., ... others (2021). What is the surface mass balance of Antarctica? An intercomparison of regional climate model estimates. *The Cryosphere*, *15*(8), 3751–3784.

Nakayama, Y., Menemenlis, D., Zhang, H., Schodlok, M., & Rignot, E. (2018). Origin of Circumpolar Deep Water intruding onto the Amundsen and Bellingshausen Sea continental shelves. *Nat. Comm.*, *9*(1), 1–9.

Nakayama, Y., Timmermann, R., Schröder, M., & Hellmer, H. H. (2014). On the difficulty of modeling Circumpolar Deep Water intrusions onto the Amundsen Sea continental shelf. *Ocean Model.*, *84*, 26–34.

Naughten, K. A., Holland, P. R., Dutrieux, P., Kimura, S., Bett, D. T., & Jenkins, A. (2022). Simulated twentieth-century ocean warming in the Amundsen Sea, West Antarctica. *Geophys. Res. Lett.*, e2021GL094566.

Naughten, K. A., Meissner, K. J., Galton-Fenzi, B. K., England, M. H., Timmermann, R., & Hellmer, H. H. (2018). Future projections of Antarctic ice shelf

melting based on CMIP5 scenarios. *J. Climate*, *31*(13), 5243–5261.
Naughten, K. A., Meissner, K. J., Galton-Fenzi, B. K., England, M. H., Timmermann, R., Hellmer, H. H., … Debernard, J. B. (2018). Intercomparison of Antarctic ice-shelf, ocean, and sea-ice interactions simulated by MetROMS-iceshelf and FESOM 1.4. *Geosci. Model Dev.*, *11*(4), 1257–1292.
Nowicki, S., Payne, A., Goelzer, H., Seroussi, H., Lipscomb, W., Abe-Ouchi, A., … van de Wal, R. (2020). Experimental protocol for sea level projections from ISMIP6 standalone ice sheet models. *The Cryosphere*, *14*, 2331–2368. doi: 10.5194/tc-14-2331-2020
Purich, A., & England, M. H. (2021). Historical and future projected warming of Antarctic Shelf Bottom Water in CMIP6 models. *Geophys. Res. Lett.*, *48*(10), e2021GL092752.
Rackow, T., Danilov, S., Goessling, H. F., Hellmer, H. H., Sein, D. V., Semmler, T., … Jung, T. (2022). Delayed Antarctic sea-ice decline in high-resolution climate change simulations. *Nature Comm.*, *13*(1), 1–12.
Rousset, C., Vancoppenolle, M., Madec, G., Fichefet, T., Flavoni, S., Barthélemy, A., … others (2015). The Louvain-La-Neuve sea ice model LIM3.6: global and regional capabilities. *Geosci. Model Dev.*, *8*(10), 2991–3005.
Seroussi, H., Nowicki, S., Payne, A. J., Goelzer, H., Lipscomb, W. H., Abe-Ouchi, A., … others (2020). ISMIP6 Antarctica: a multi-model ensemble of the Antarctic ice sheet evolution over the 21st century. *The Cryosphere*, *14*(9), 3033–3070.
Siahaan, A., Smith, R., Holland, P., Jenkins, A., Gregory, J. M., Lee, V., … Jones, C. (2021). The Antarctic contribution to 21st century sea-level rise predicted by the UK Earth System Model with an interactive ice sheet. *The Cryosphere Discussions*, 1–42.
Smith, R. S., Mathiot, P., Siahaan, A., Lee, V., Cornford, S. L., Gregory, J. M., … others (2021). Coupling the UK Earth System Model to dynamic models of the Greenland and Antarctic ice sheets. *J. Adv. Model. Ea. Sys.*, *13*(10), e2021MS002520.
Spence, P., Griffies, S. M., England, M. H., Hogg, A. M., Saenko, O. A., & Jourdain, N. C. (2014). Rapid subsurface warming and circulation changes of Antarctic coastal waters by poleward shifting winds. *Geophys. Res. Lett.*, *41*(13), 4601–4610.
Stewart, A. L., Klocker, A., & Menemenlis, D. (2018). Circum-Antarctic Shoreward Heat Transport Derived From an Eddy-and Tide-Resolving Simulation. *Geophys. Res. Lett.*, *45*(2), 834–845. doi: 10.1002/2017GL075677
St-Laurent, P., Klinck, J. M., & Dinniman, M. S. (2013). On the role of coastal troughs in the circulation of warm Circumpolar Deep Water on Antarctic shelves. *J. Phys. Oceanogr.*, *43*(1), 51–64.
Swart, N. C., & Fyfe, J. C. (2012). Observed and simulated changes in the Southern Hemisphere surface westerly wind-stress. *Geophys. Res. Lett.*, *39*(16).
Timmermann, R., & Hellmer, H. H. (2013). Southern Ocean warming and increased ice shelf basal melting in the twenty-first and twenty-second centuries based on coupled ice-ocean finite-element modelling. *Ocean Dyn.*, *63*(9-10), 1011–1026.
van Westen, R. M., & Dijkstra, H. A. (2021). Ocean eddies strongly affect global mean sea-level projections. *Science Adv.*, *7*(15), eabf1674.
Williamson, D. B., Blaker, A. T., & Sinha, B. (2017). Tuning without over-tuning: parametric uncertainty quantification for the NEMO ocean model. *Geosci. Model Dev.*, *10*(4), 1789–1816.

Supporting Information for "Ice shelf basal melt rates in the Amundsen Sea at the end of the 21st century"

Nicolas C. Jourdain[1], Pierre Mathiot[1], Clara Burgard [1], Justine Caillet[1],

Christoph Kittel[1]

[1]Univ. Grenoble Alpes/CNRS/IRD/G-INP, Institut des Géosciences et de l'Environnement, Grenoble, France

Contents of this file

1. Supplementary sections S1 to S4.
2. Figures S1 to S6.
3. Table S1.

Corresponding author: N. C. Jourdain, Institut des Géosciences de l'Environnement, University Grenoble Alpes, CS 40700, 38 058 Grenoble Cedex 9, France. (nicolas.jourdain@univ-grenoble-alpes.fr)

Introduction

Here we present additional diagnostics that help support the main manuscript. They include comparison of our simulations to observational estimates (section S1), a description of future changes regarding sea ice, Ekman pumping and the surface buoyancy fluxes (section S2), a description of the future anomalies applied at the model lateral boundaries (section S3), and a description of the heat and salt budgets northward of the Amundsen continental shelf (section S4).

S1. Evaluation of the present day simulations

We first evaluate the vertical temperature and salinity profiles in front of the most important ice shelf cavities (Fig. S1). The observations come from in-situ Condictivity-Temperature-Depth (CTD) measurements over 1994-2018 (Dutrieux et al., 2014; Jenkins et al., 2018). The three model ensemble members (A, B, C) have slightly different properties (e.g., C is less stratified), but their biases with respect to observations are very similar. NEMO generally has a warm bias below the thermocline, of approximately 0.5°C for Pine Island, Thwaites and Getz, and up to 1°C for Dotson. The model thermocline tends to be too shallow, and the bias is particularly strong for Getz where the model thermocline is $\sim$200 m above the observed one.

We then evaluate the simulated cavity melt rates in comparison to oceanographic and remote-sensing observational estimates (Fig. S2). The simulated melt rate at Pine Island is in good agreement with observational estimates. Thwaites melt rates appear strongly under-estimated, but its recent geometry is used in our simulations while observational estimates were done before its partial collapse. For the other ice shelves, simulated melt rates are overestimated, consistently with the aforementioned warm bias at depth. The melt bias is particularly important for Getz because the overly shallow thermocline at its front exposes large areas of ice to modified circumpolar deep water instead of surface water.

S2. Future changes in sea ice cover, Ekman pumping and buoyancy fluxes

Here we describe the changes at the ocean surface, first in terms of sea ice concentration and thickness, then in terms of Ekman pumping and surface buoyancy fluxes which are the main external drivers of changes in the ocean circulation.

Nearly 90% of the present-day austral summer (January to March) sea ice concentration over the Amundsen Sea continental shelf disappears in the future (Fig. S3a,b). There is a strong retreat of the main sea ice front in austral winter, but the sea ice concentration remains mostly unchanged between the present and the future over the Amundsen continental shelf (Fig. S3c,d). The winter sea ice thickness is nonetheless reduced, from 1.28 m on average for present day to 0.85 m in the future over the continental shelf (Fig. S3e,f). The annual net sea ice production over the continental shelf (which matters for ocean convection) decreases from 231 $\mathrm{Gt\,yr^{-1}}$ presently to 194 $\mathrm{Gt\,yr^{-1}}$ in the future (not shown).

The Ekman vertical velocity (w_E) is calculated as:

$$w_E = -\frac{1}{\rho_w} \nabla \times \left(\frac{\vec{\tau}}{f} \right) \tag{1}$$

where ρ_w is the seawater density (1028 kg.m^{-3}), τ the ocean surface friction (exerted by wind and sea ice), and f the Coriolis parameter. The multiple dipole-like structures in the Ekman velocity (Fig. S4a) correspond to relatively intense surface currents that feel the sea ice drag, with opposite friction curl on either side of the currents. These dipoles tend to be weakened in the future (Fig. S4b), possibly because of the reduced sea ice cover and thickness. On average, the Amundsen continental shelf experiences an Ekman downwelling (see number in Fig. S4a) that is reduced by half in the future simulations (see number in Fig. S4b).

The surface buoyancy flux is calculated as:

$$B = \frac{g}{c_{pw}} \alpha_{T,S} Q + g S \beta_{T,S} F \tag{2}$$

where g is the gravity acceleration (9.81 $\mathrm{m\,s^{-2}}$), c_{pw} the seawater specific heat capacity (3992 $\mathrm{J\,K^{-1}\,kg^{-1}}$), T and S the conservative temperature and absolute salinity at the ocean surface, $\alpha_{T,S}$ the thermal expansion coefficient at constant salinity, $\beta_{T,S}$ the saline contraction coefficient at constant temperature, Q the net heat flux received by the ocean surface (from the atmosphere and sea ice), and F the net freshwater flux at the ocean surface, positively influenced by precipitation, iceberg melt, sea ice melt and runoff (neglected in our study), and negatively influenced by evaporation and sea ice formation. On average, for present day, the Amundsen Sea is loosing surface buoyancy (Fig. S4c), which is due to sea ice production, particularly in coastal polynyas, which is not fully compensated by sea ice melt as the later occurs further offshore due to sea ice drift. In the future, less sea ice is produced and there is more precipitation, which weakens the annual buoyancy loss by 75% on average for the Amundsen Sea (Fig. S4d).

S3. Future ocean changes at the lateral boundaries

Here we describe the ocean perturbation applied at the lateral boundaries of our ocean model configuration as it significantly impacts future ice shelf melt rates.

The ocean warming imposed at the lateral boundaries generally exceeds 0.25°C in the first 1000 m and 0.5°C in the first 500 m (Fig. S5a). This is approximately in agreement with the 0.4°C warming of Circumpolar Deep Water (CDW) in the CMIP5 multi-model mean under RCP8.5 (Sallée et al., 2013). As argued by Sallée et al. (2013), vertical mixing is likely responsible for such warming because advection from the CDW formation regions is expected to take several centuries. The imposed warming is also slightly stronger throughout the water column on the continental shelf on both sides of the lateral boundaries, with warming amplitude consistent with the +0.66°C reported by Little and Urban (2016) for the Amundsen Sea under RCP85. This may indicate some additional Ekman dynamics (reduced downwelling) related to poleward shifted westerlies in the future (Spence et al., 2014).

A slight freshening of the first 100 m is also imposed along most of the lateral boundaries (Fig. S5b), with a weak signal also reported by Sallée et al. (2013). The anomaly is much stronger and deeper on the continental shelf on both sides of the lateral boundaries, exceeding -0.3 and -0.6 $g.kg^{-1}$ at the western and eastern boundaries, respectively. The deep vertical structure is again consistent with reduced downwelling in response to poleward shifted winds (Spence et al., 2014). This freshening signal near Antarctica is also likely related to the increased glacial freshwater flux from the Antarctic ice sheet (the later was crudely represented in CMIP5; for example, some modelling centers increased the glacial freshwater fluxes into the Southern Ocean to instantaneously compensate for greater snow accumulation over the ice sheet in a warmer climate).

In terms of perturbed ocean velocities, we find a westward anomaly near the continental shelf, as previously reported by Wang (2013). The anomaly structure is similar to the typical Antarctic Slope Current. The relatively weak anomalies probably result from the large spread of dynamical responses across the CMIP5 models (Wang, 2013; Meijers et al., 2012).

S4. Estimation of future iceberg melt rates

The ISMIP6 results indicate that for each 1 Gt of additional melt beneath the East-Amundsen ice shelves (Cosgrove, Pine Island, Thwaites, Crosson and Dotson) there will be 0.72 Gt of additional calving from these ice shelves (Seroussi et al., 2020, , their Fig. 15). For Getz ice shelf, each 1 Gt of additional melt induces 0.18 Gt of additional calving. We apply these sensitivities to the increased ice-shelf basal melt rates in our simulations and deduce an increase in calving rates (2nd part of Tab. S1). With respect to the present-day values of Depoorter et al. (2013), this corresponds to 67 to 103% of additional calving in the Crosson-Dotson sector, and to 39 to 64% of additional ice calved by Getz (3rd part of Tab. S1).

Analysing the tracks of Lagrangian icebergs in the global 0.25° simulation used as lateral boundary conditions of our regional simulations, we find that only 14% of the iceberg mass calved in the Amundsen Sea does melt in the Amundsen Sea. Most of them actually melt farther away, in the Antarctic Circumpolar Current. It means that the total iceberg melt flux in the Amundsen Sea is not only controlled by the calving rate, but also by the melt intensity when icebergs travel across the Amundsen Sea. To estimate the effect of more intense melting, we use the iceberg model equations (Martin & Adcroft, 2010) and consider that surface water temperatures increase from -1.5°C to -1.0°C (based on our NEMO simulations). The response is dominated by increased wave erosion (+100%), while increased melting at the iceberg base (+20%) is nearly compensated by decreased convection along the iceberg side walls (-26%). We note that the equation provided by Martin and Adcroft (2010) for melt induced by convection along the iceberg side walls may not be realistic for negative ocean temperatures and should probably be based on the ocean salinity, but this term does not have an important impact on our overall estimate.

Therefore, we estimate that the relative increase in iceberg melt rate compared to present-day (4th part of Tab. S1) is the sum of the relative increase in calving and of the relative increase in wave erosion. The maximum response across the 3 ensemble members is an additional 203% melting for icebergs coming from the Cosgrove-Dotson sector and an additional 164% for icebergs coming from Getz.

As we saved the original iceberg melt flux per sector of origin, we are able to multiply by 3.03 the pattern of iceberg melt coming from the Eastern Amundsen Sea and by 2.64 the pattern of iceberg melt coming from the Western Amundsen Sea. This affects only 44% of the present-day iceberg melt flux in the Amundsen Sea as 41% comes from icebergs calved in the Bellingshausen Sea, 12% come from the Ross Sea, and 3% from the Adélie Land (estimates for the Amundsen continental shelf between 135°W and 100°W). We assume that these other sectors do not change in the future because there is a weaker calving to basal melt relationship compared to Amundsen sector (Seroussi et al., 2020), and because increased iceberg erosion by the ocean may decrease their ability to be transported far away. The resulting total iceberg melt flux over the Amundsen continental shelf increases from 63 Gt yr−1 at present-day to 136 Gt.yr^{-1} at the end of the 21st century under RCP85.

S5. Description of the offshore projected changes

Here we analyse the offshore properties and the terms of the exact heat and salt budget (saved online and calculated as in Jourdain et al., 2017) to get further insights into the physical mechanisms. Northward of the Amundsen continental shelf (i.e., north of the 1500 m isobath and south of 69°S, and between 100°W and 135°W), we project a surface ocean warming of 1°C (Fig. S6a), mostly explained by stronger downward heat fluxes (Fig. S6c), as well as a surface freshening of 0.4 g kg^{-1} (Fig. S6b) explained by increased precipitation and possibly less sea ice production (Fig. S6d). The main thermocline is approximately 75 m higher in the future (Fig. S6a), which comes from reduced convective mixing due to less brine rejection as well as horizontal advection (Fig. S6c,d). The ocean below the thermocline is warmed by approximately 0.25°C in the future (Fig. S6a), which is largely explained by horizontal advection from the domain boundaries (Fig. S6c). In comparison, Sallée et al. (2013) reported that the Circumpolar Deep Water warmed by 0.4°C from 1976-2005 to 2070-2099 in the CMIP5-RCP8.5 multi-model mean.

References

Adusumilli, S., Fricker, H. A., Medley, B., Padman, L., & Siegfried, M. R. (2020). Interannual variations in meltwater input to the Southern Ocean from Antarctic ice shelves. *Nature Geosci.*, *13*(9), 616–620.

Depoorter, M. A., Bamber, J. L., Griggs, J. A., Lenaerts, J. T. M., Ligtenberg, S. R. M., van den Broeke, M. R., & Moholdt, G. (2013). Calving fluxes and basal melt rates of Antarctic ice shelves. *Nature*, *502*(7469), 89–92.

Dutrieux, P., De Rydt, J., Jenkins, A., Holland, P. R., Ha, H. K., Lee, S. H., ... Schröder, M. (2014). Strong sensitivity of Pine Island ice-shelf melting to climatic variability. *Science*, *343*(6167), 174–178.

Jenkins, A., Shoosmith, D., Dutrieux, P., Jacobs, S., Kim, T. W., Lee, S. H., ... Stammerjohn, S. (2018). West Antarctic Ice Sheet retreat in the Amundsen Sea driven by decadal oceanic variability. *Nature Geosc.*, *11*, 733–738.

Joughin, I., Shapero, D., Dutrieux, P., & Smith, B. (2021). Ocean-induced melt volume directly paces ice loss from Pine Island Glacier. *Science advances*, *7*(43), eabi5738.

Jourdain, N. C., Mathiot, P., Merino, N., Durand, G., Le Sommer, J., Spence, P., ... Madec, G. (2017). Ocean circulation and sea-ice thinning induced by melting ice shelves in the Amundsen Sea. *J. Geophys. Res. Oceans*, *122*(3), 2550–2573.

Little, C. M., & Urban, N. M. (2016). CMIP5 temperature biases and 21st century warming around the Antarctic coast. *Ann. Glaciol.*, *57*(73), 69–78.

Martin, T., & Adcroft, A. (2010). Parameterizing the fresh-water flux from land ice to ocean with interactive icebergs in a coupled climate model. *Ocean Model.*, *34*(3), 111–124.

Meijers, A. J., Shuckburgh, E., Bruneau, N., Sallée, J.-B., Bracegirdle, T. J., & Wang, Z. (2012). Representation of the Antarctic Circumpolar Current in the CMIP5 climate models and future changes under warming scenarios. *J. Geophys. Res. Oceans*, *117*(C12).

Rignot, E., Jacobs, S., Mouginot, J., & Scheuchl, B. (2013). Ice-shelf melting around

Antarctica. *Science*, *341*(6143), 266–270.

Sallée, J. B., Shuckburgh, E., Bruneau, N., Meijers, A. J., Bracegirdle, T. J., Wang, Z., & Roy, T. (2013). Assessment of Southern Ocean water mass circulation and characteristics in CMIP5 models: Historical bias and forcing response. *J. Geophys. Res. Oceans*, *118*(4), 1830–1844.

Seroussi, H., Nowicki, S., Payne, A. J., Goelzer, H., Lipscomb, W. H., Abe-Ouchi, A., ... others (2020). ISMIP6 Antarctica: a multi-model ensemble of the Antarctic ice sheet evolution over the 21st century. *The Cryosphere*, *14*(9), 3033–3070.

Spence, P., Griffies, S. M., England, M. H., Hogg, A. M., Saenko, O. A., & Jourdain, N. C. (2014). Rapid subsurface warming and circulation changes of Antarctic coastal waters by poleward shifting winds. *Geophys. Res. Lett.*, *41*(13), 4601–4610.

Wang, Z. (2013). On the response of Southern Hemisphere subpolar gyres to climate change in coupled climate models. *J. Geophys. Res. Oceans*, *118*(3), 1070–1086.

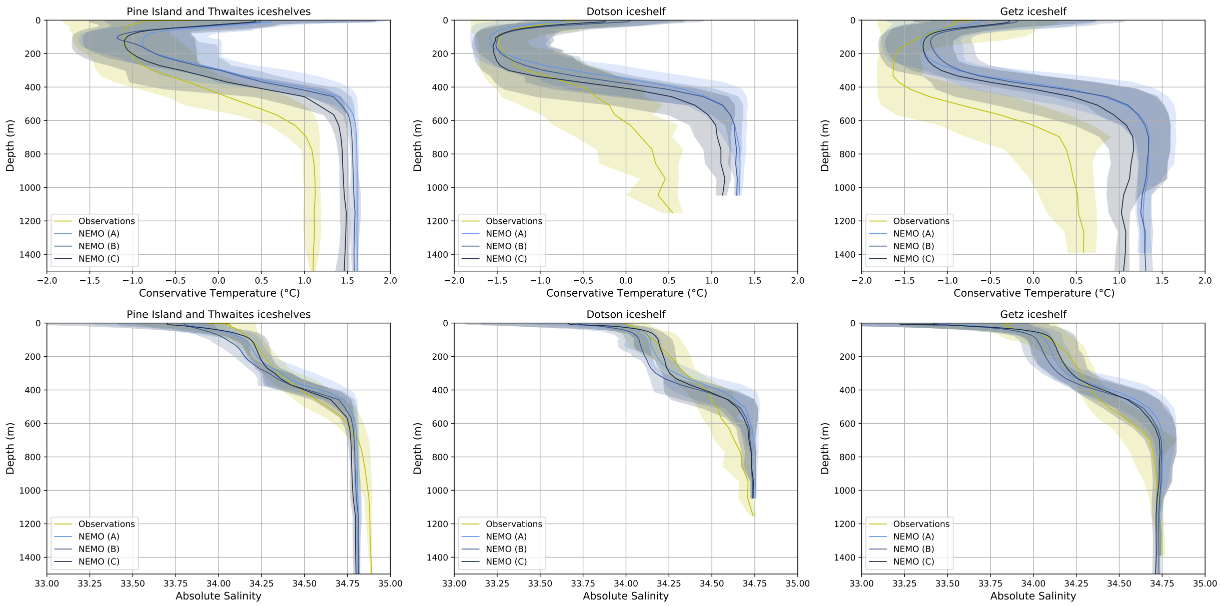

Figure S1. Vertical temperature and salinity profiles averaged in front of Pine Island and Thwaites (108-100°W, 76-74°S), Dotson (114-111°W, 75-73°S) and Getz (135-114°W, 75-73°S, over the continental shelf) from observational data (see text) and model configurations A, B and C. The model profiles are co-located in space and time with the observational profiles (linear interpolations based on monthly model outputs). The shaded semi-transparent areas indicate the 5th and 95th percentiles over all co-located profiles.

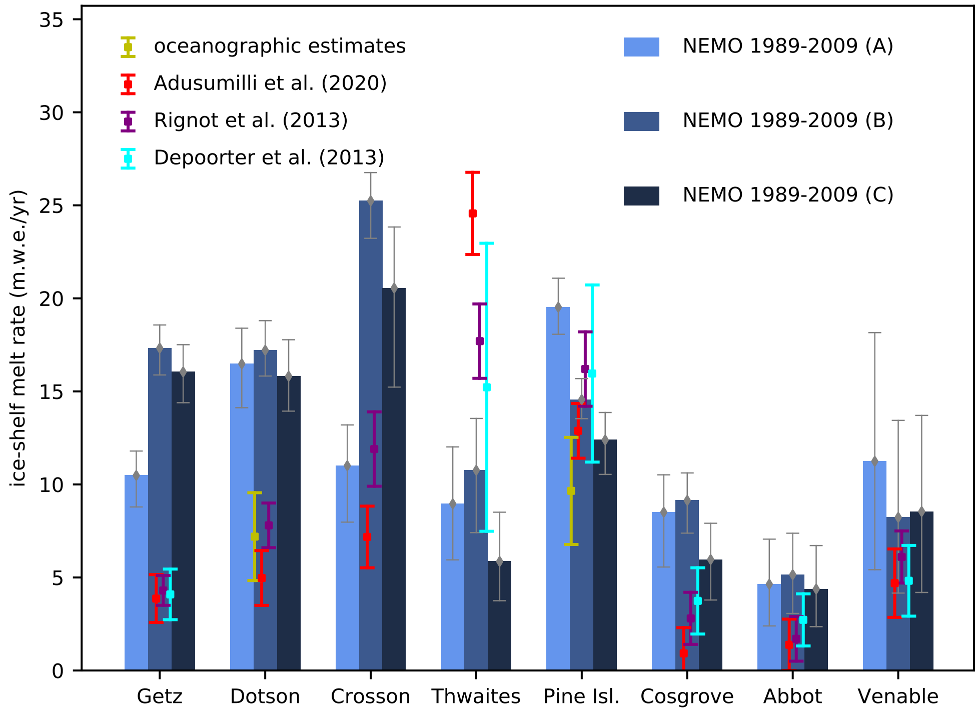

Figure S2. Comparison of simulated (large blue bars) and observation-based (thin colored bars) melt rates beneath individual ice shelves. Oceanographic estimates represent summers of early 1994, 2007, 2009, 2010, 2012, and 2014 for Pine Island (Joughin et al., 2021) and summers of early 2000, 2006, 2007, 2009, 2011, 2012, 2014 and 2016 for Dotson (Jenkins et al., 2018). The other observational estimates are based on satellite observations combined with firm simulations and represent the 2003-2008 period for Rignot et al. (2013) and Depoorter et al. (2013) and 1994-2018 for Adusumilli et al. (2020). The observational error bars show the 95% confidence interval based on 10^6 calculations of the multi-year mean, using random samples in normal distributions for individual years with standard deviations provided by Joughin et al. (2021) and Jenkins et al. (2018). The 95% interval for Rignot et al. (2013) and (Depoorter et al., 2013) was calculated from the provided standard deviation assuming a normal distribution. Grey bars indicate 95% of model monthly outputs (i.e. leaving out the 2.5% lowest and 2.5% highest values).

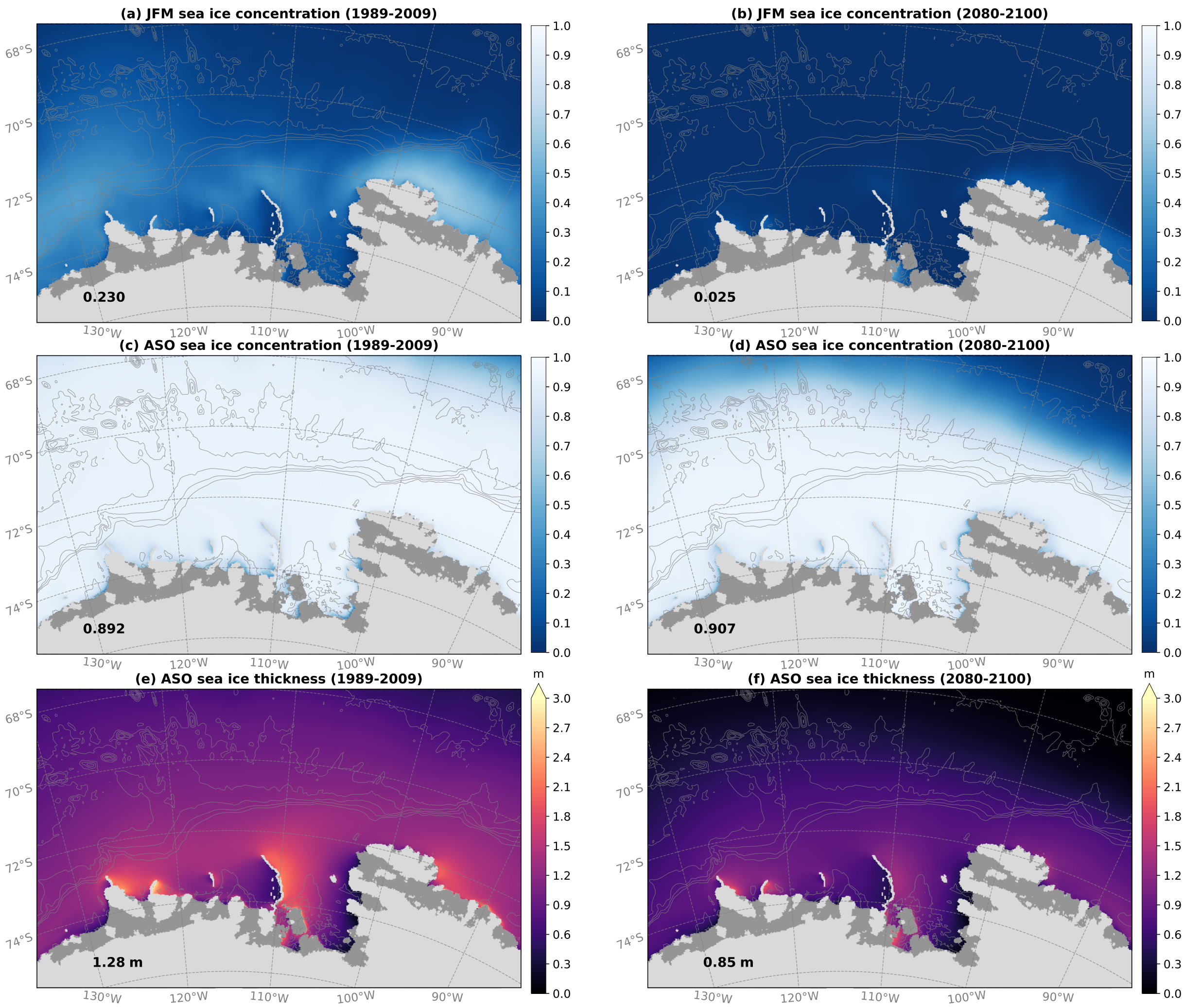

Figure S3. Sea ice concentration and thickness in austral summer (JFM) and late austral winter (ASO) for present day and future simulations. Numbers near the lower left corner indicate values integrated over the continental shelf defined as the area between the 1500 m isobath and the coastline, and between 100°W and 135°W.

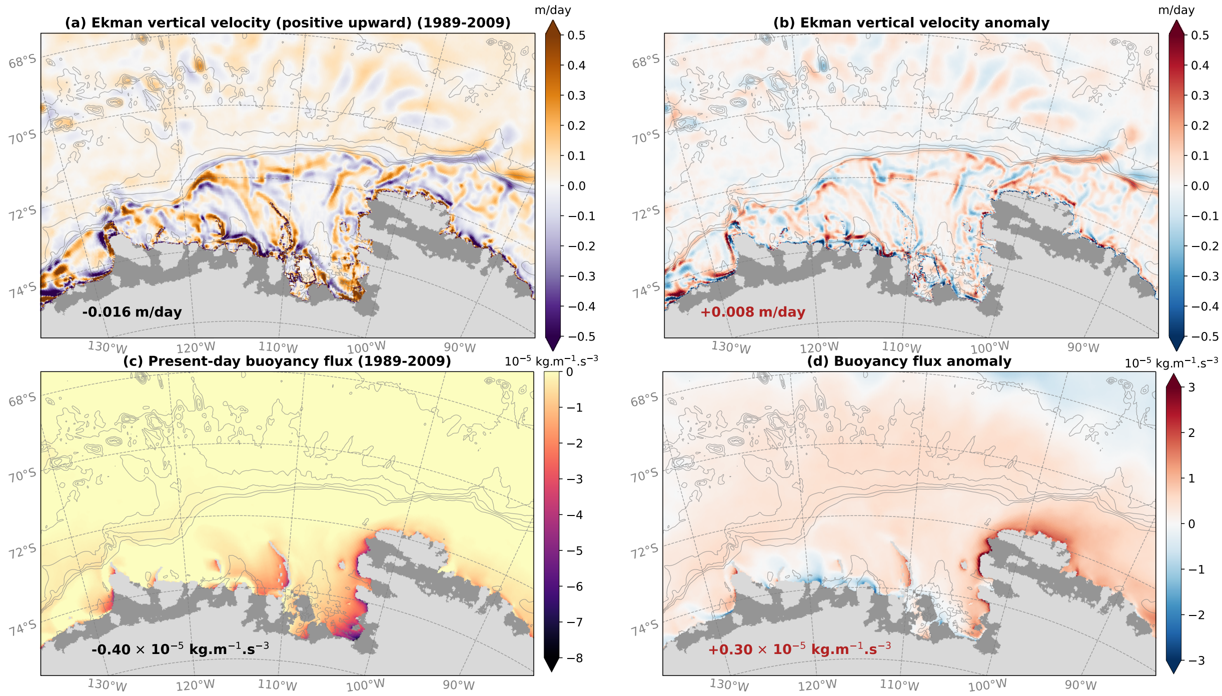

Figure S4. Present-day (left) and future anomaly (2080–2100 minus 1989–2009) of Ekman vertical velocity (upper) and surface buoyancy flux (lower). Numbers near the lower left corner indicate values averaged over the continental shelf defined as the area between the 1500 m isobath and the coastline, and between 100°W and 135°W.

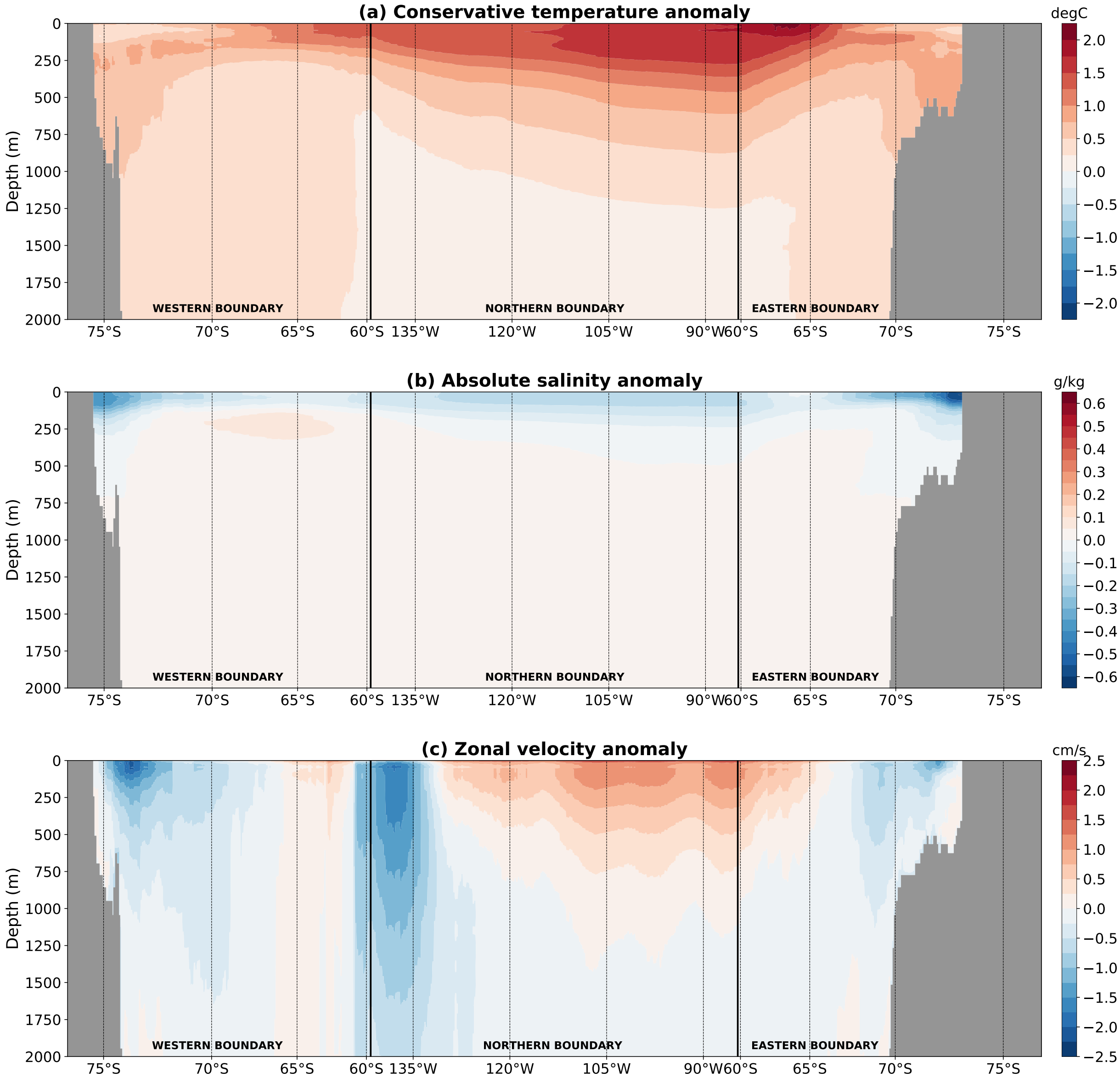

Figure S5. CMIP5 multi-model mean anomalies added to the present-day lateral boundary conditions of (a) conservative temperature, (b) absolute salinity, and (c) zonal ocean velocity. The model bathymetry is shown in grey and only the first 2000 m are shown.

Table S1. Changes in ice shelf melt rates found in NEMO simulations A, B and C (1st part), and subsequent increase in calving rate according to the ISMIP6 sensitivity (2nd part). Relative increase in calving rate compared to present-day (3rd part) and relative increase in iceberg melt due to both increased calving and increased erosion by a warmer ocean (4th part).

	A	**B**	**C**
Increase in ice shelf melt (Gt.yr^{-1})			
Crosson–Dotson	+174	+124	+189
Getz	+121	+156	+199
Increase in iceberg calving (Gt yr^{-1})			
Crosson–Dotson	+125	+89	+136
Getz	+22	+28	+36
Relative increase in calving			
Crosson–Dotson	+95%	+67%	+103%
Getz	+39%	+59%	+64%
Relative increase in iceberg melt			
Crosson–Dotson	+195%	+167%	+203%
Getz	+139%	+159%	+164%

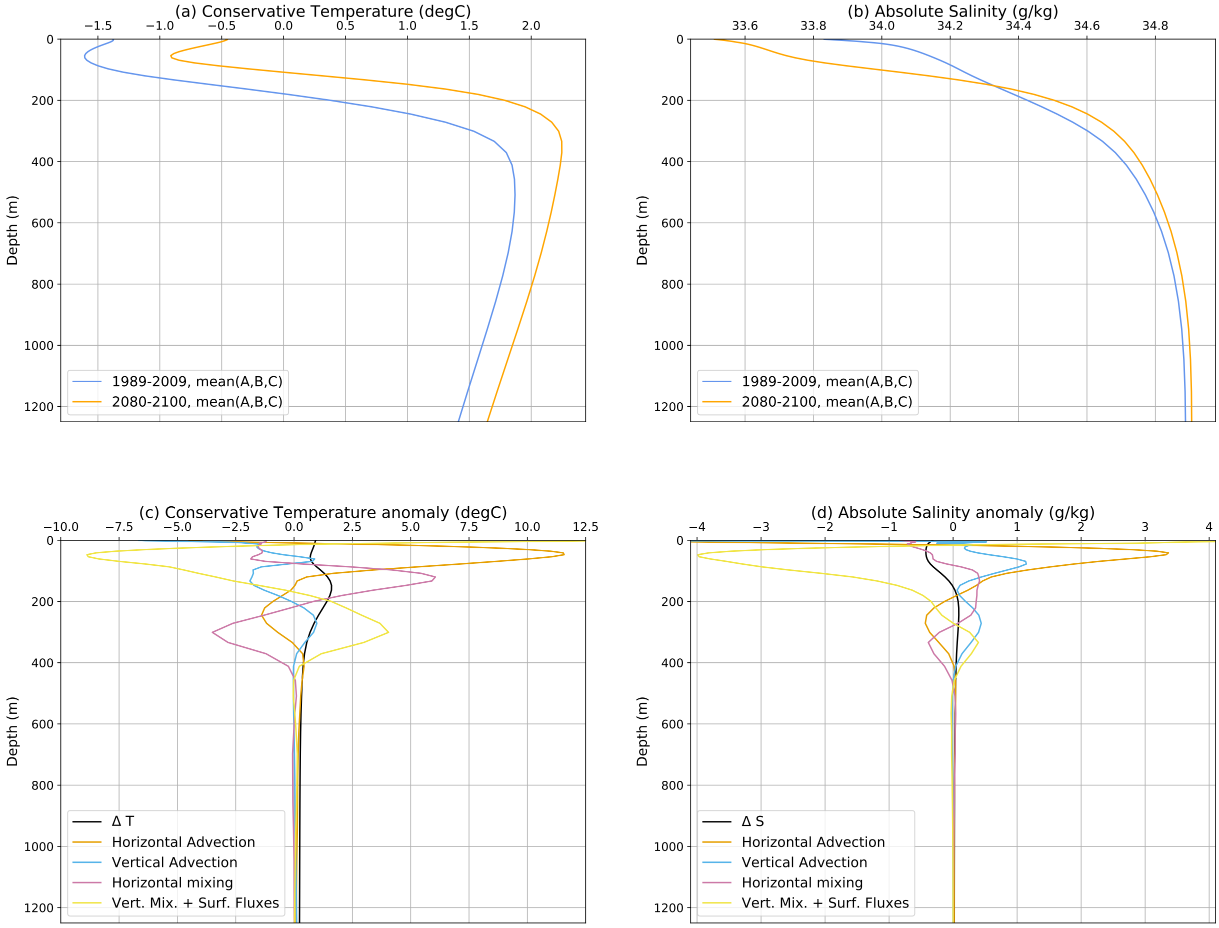

Figure S6. (a,b) Present-day and future conservative temperature and absolute salinity profiles offshore of the Amundsen Sea continental shelf (average north of the 1500 m isobath and south of 69°S, and between 100°W and 135°W). (c,d) temperature (ΔT) and salinity (ΔS) change from present-day to future conditions and contributions of the individual terms of the heat and salt equations to ΔT and ΔS, respectively.